学 位 論 文

Three- dimensional Reconstruction by Tilt Series of Electron Micrographs
from Thin Sections of Contracting Skeletal Muscle Fibres

収縮中骨格筋の超薄切片からの電子顕微鏡傾斜像シリーズによる三次元再構成

平成5年12月 博士（理学）申請

東京大学大学院理学系研究科 物理学専攻

光 岡 薫

Three-dimensional Reconstruction by Tilt Series of Electron Micrographs from Thin Sections of Contracting Skeletal Muscle Fibres

Kaoru Mitsuoka

December 27, 1993

submitted to School of Science, University of Tokyo
as a doctor thesis

Contents

1

Abstract

For the better understanding of the molecular mechanism of muscle contraction, I investigated the three-dimensional structure of the cross-bridges of contracting skeletal muscle fibres.

By rapid-freezing and freeze-substitution technique, clear images of cross-bridges during isometric contraction were obtained. I took tilt series of the same region of an ultra-thin section of a contracting muscle fibre. The tilting angles of a section are $0°$, $±15°$, $±30°$, $±45°$, and $±60°$, respectively. I tilted sections around each of two tilting axes that are almost perpendicular to each other.

To reduce the radiation damage, I used Imaging Plate (IP) which is very sensitive recording media with wide dynamic range. The total electron dosage of the region in which the tilt series were observed was under $20 \ e/\text{Å}$.

For image reconstruction by back-projection method, I corrected the tilt angles of planes of the sections from the coordinates of fiducial markers. To normalize the densities of each image, I unified the densities of images of the tilt series by modelling histograms of images on two Gaussian curves. Then I multiplied the constant values according to the corrected tilting angles of the images, assuming the uniform distribution of densities of proteins. With simple back-projection technique, I could reconstruct three-dimensional images of contracting muscle fibres.

To increase the signal-to-noise ratio of the reconstructed three-dimensional images, I used median filtering. The area to calculate median was determined to be a cubic of 4 nm radius from the resolution of the reconstructed image. The resolution was estimated by the difference between the reconstructed image and the observed images. In this process, the effect of radiation damage was also examined. Resolution was estimated to be 4-8 nm and no significant radiation damage was found.

By this filtering procedure, the contoured maps of reconstructed images could be obtained. In these views, the thick filaments in contracting a muscle fibre could be clearly seen. Also cross-bridges between thin and thick filaments could be observed. 'Tadpole'-like cross-bridges observed in muscle fibres in rigor state were observed, although many cross-bridges of different shapes could be distinguished.

The cross-bridges protrude from thick filaments to thin filaments without particular inclined direction in a plane perpendicular to the axis of thick fila-

ments. The number of cross-bridges observed in the reconstructed images was about 1/3 of all the myosin molecules. This is consistent with the model of muscle contraction that was proposed by A. F. Huxley in 1957, In this model, about 1/5 of all myosin heads are associated strongly with thin filaments, because each myosin molecule has two head regions.

In this way, three-dimensional images of cross-bridges in contracting muscle fibres could be reconstructed. From these images, some features that cannot be obtained from images in projection are discussed. Also, these images were compared with other three-dimensional images in the static state but with better resolutions.

Abbreviations

ATP adenosine tri-phosphate

DDSA dodecenyl succinic anhydride

EGTA ethyleneglycol bis-(2-aminoethylether) tetraacetic acid

IP Imaging Plate

PIPES piperazine-N,N'-bis-(2-ethanesulfonic acid)

MNA methyl nadic anhydride

RDW re-distilled water

S1 myosin subfragment-1

S.D. standard deviation

1 Introduction

Muscle contraction occurs when two sets of filaments, the myosin-containing thick filaments and the actin-containing thin filaments, slide past each other (Huxley,A.F. & Niedergerke,R. 1954; Huxley,H.E. & Hanson,J. 1954). The force which produces filament motion is generated by the interaction of cross-bridges and thin filaments (Huxley,A.F., 1957; Huxley,H.E., 1969). A widely accepted theory to explain this force-generating process is the cross-bridge hypothesis of muscle contraction whereby sliding is brought about by cross-bridges that extend from myosin filaments and interact cyclically in a rowing motion with actin filaments as adenosine triphosphate (ATP) is hydrolyzed (Huxley,A.F. & Simmons,R.M., 1971).

Recently, the atomic structure of these two proteins, actin and myosin, has been solved by X-ray crystallography (Kabsch,W., *et al.*, 1990; Rayment,I., *et al.*, 1993). By combining the molecular structure of the individual proteins with low-resolution electron density maps of the complex derived from cryo-electron microscopy and image analysis, a model structure for the rigor complex, in which myosin heads are attached to actin filaments, was obtained. From this structure, a model for the molecular basis of muscle contraction was proposed (Rayment,I., *et al.*, 1993). In this model, the spatial relation between the ATP binding pocket of myosin head and the major contact area on actin suggests a working hypothesis for the cross-bridge cycle that is consistent with previous several independent structural and biochemical studies.

However, some experimental results, which appear to conflict with this model, also are reported. For example, the sliding distance of an actin filament induced by one ATP hydrolysis cycle was obtained by several methods, and it has been estimated over 40–100 nm, that is much bigger than the diameter of myosin subfragment 1 (S1) molecule (Harada,Y., *et al.*, 1992; Higuchi,H. & Goldman,Y.E., 1991), while it is controversial (Uyeda,T.Q.P., *et al.*, 1990). Also, the structural changes of S1 molecule and their angular changes of alignment in the contracting muscle fibres has not been fully understood (Cooke,R. *et al.*, 1982; Yanagida,T., 1981), while static structure of myosin S1 molecules solved by electron microscopy (Toyoshima,C. & Wakabayashi,T., 1979) and they were related to structural changes of them (Toyoshima,C. & Wakabayashi,T., 1985a; Toyoshima,C. & Wakabayashi,T., 1985b). Recently some evidence of structural changes of S1 *in vitro* have been emerged (Wakabayashi,K. *et al.*, 1992; Katayama,E., 1989).

Abbreviations

ATP adenosine tri-phosphate

DDSA dodecenyl succinic anhydride

EGTA ethyleneglycol bis-(2-aminoethylether) tetraacetic acid

IP Imaging Plate

PIPES piperazine-N,N'-bis-(2-ethanesulfonic acid)

MNA methyl nadic anhydride

RDW re-distilled water

S1 myosin subfragment-1

S.D. standard deviation

1   Introduction

Muscle contraction occurs when two sets of filaments, the myosin-containing thick filaments and the actin-containing thin filaments, slide past each other (Huxley,A.F. & Niedergerke,R. 1954; Huxley,H.E. & Hanson,J. 1954). The force which produces filament motion is generated by the interaction of cross-bridges and thin filaments (Huxley,A.F., 1957; Huxley,H.E., 1969). A widely accepted theory to explain this force-generating process is the cross-bridge hypothesis of muscle contraction whereby sliding is brought about by cross-bridges that extend from myosin filaments and interact cyclically in a rowing motion with actin filaments as adenosine triphosphate (ATP) is hydrolyzed (Huxley,A.F. & Simmons,R.M., 1971).

Recently, the atomic structure of these two proteins, actin and myosin, has been solved by X-ray crystallography (Kabsch,W., *et al.*, 1990; Rayment,I., *et al.*, 1993). By combining the molecular structure of the individual proteins with low-resolution electron density maps of the complex derived from cryo-electron microscopy and image analysis, a model structure for the rigor complex, in which myosin heads are attached to actin filaments, was obtained. From this structure, a model for the molecular basis of muscle contraction was proposed (Rayment,I., *et al.*, 1993). In this model, the spatial relation between the ATP binding pocket of myosin head and the major contact area on actin suggests a working hypothesis for the cross-bridge cycle that is consistent with previous several independent structural and biochemical studies.

However, some experimental results, which appear to conflict with this model, also are reported. For example, the sliding distance of an actin filament induced by one ATP hydrolysis cycle was obtained by several methods, and it has been estimated over 40–100 nm, that is much bigger than the diameter of myosin subfragment 1 (S1) molecule (Harada,Y., *et al.*, 1992; Higuchi,H. & Goldman,Y.E., 1991), while it is controversial (Uyeda,T.Q.P., *et al.*, 1990). Also, the structural changes of S1 molecule and their angular changes of alignment in the contracting muscle fibres has not been fully understood (Cooke,R. *et al.*, 1982; Yanagida,T., 1981), while static structure of myosin S1 molecules solved by electron microscopy (Toyoshima,C. & Wakabayashi,T., 1979) and they were related to structural changes of them (Toyoshima,C. & Wakabayashi,T., 1985a; Toyoshima,C. & Wakabayashi,T., 1985b). Recently some evidence of structural changes of S1 *in vitro* have been emerged (Wakabayashi,K. *et al.*, 1992; Katayama,E., 1989).

To give clear answers for complex situation like this, it is crucial to know file three-dimensional structure of cross-bridges during contraction. Using the three-dimensinal structure, they can be correlated with chemical states of myosin and actomyosin complexes (Eisenberg,E. & Hill,T.L., 1985). Technical advance of rapid-freezing and freeze-substitution method (Heuser,J.E., *et al.*, 1979) enabled us to observe time-resolved structure by electron microscopy. From the observation of sections of rapidly-frozen rabbit glycerinated fibres, it was reported that cross-bridges in contracting muscle are arranged with the axial spacing of 14.3 nm and are angled closer to 90° than in rigor cross-bridges (Tsukita,S. & Yano,M., 1985; Hirose,K. & Wakabayashi,T., 1993). Lately, this technique was coupled with caged ATP (Funatsu,T., *et al.*, 1993; Hirose,K., *et al.*, 1993), and the structures of cross-bridges could be correlated with their chemical states, although these observations are two-dimensional. In projected two-dimensional views, it is difficult to observe structure of cross-bridges, because they and thin filaments overlap in those projected views. Thus the qualitative measurement of sturucture of cross-bridges and their comparison to atomic structure of myosin S1 are difficult.

To compare the atomic structures with the fine structure obtained by electron microscopy, the three-dimensional reconstruction is necessary. I used the rapid-freezing and freeze-substitution method to observe the structure of muscle fibres in contraction. By this method I could reconstruct three-dimensional images of cross-bridges from a portion of a muscle fibre. In this scheme, I did not average different cross-bridges to calculate the reconstructed images. Although the resolution of reconstructed images without averaging is limited to several nanometre, we could observe the various types of three-dimensional images of cross-bridges. They may correspond to the various chemical states, while qualitative classification must be done for correlating these shapes to chemical states.

2 Materials and Methods

2.1 Preparations of Glycerinated Muscle Fibres

As a sample, glycerinated psoas fibres of rabbit were used. The glycerinated fibres were prepared in usual way as below. Rabbit psoas fibres were immersed in 50% glycerin / relaxation(104.4 mM potassium methanesulphonate, 5.4 mM magnesium methanesulphonate, 4.2 mM ATP, 10 mM EGTA, 20 mM PIPES, pH 7.0) solutions for over a day and stored at -20 °C in a freezer (Szent-Gyorgyi,A., 1951).

Before use, the solutions were replaced to 25%, 12.5%, 0% glycerin and relaxation solutions to remove glycerin. (This was done after the temperature of solutions was back to the room temperature.) In each steps, the muscle fibres were immersed in each solutions for over 1 hour. These muscle fibres was separated to small bundles(0.3–0.5 mm in diameter, 10 mm in length) in relaxation solution.

2.2 Rapid-Freezing and Freeze-Substitution of Specimens

Contracting muscle fibres was rapidly frozen. In this experiment, muscle fibres were isometrically contracting. To fix the two ends of the small bundle, T-shaped aluminum film was used (Figure 3). The small bundles was hold by the aluminum clips which are tied to a cotton thread to fix in one end and to connect a transducer in the other end on a sample holder. Then the small bundles of muscle fibres on the sample holder was immersed in the pre-activation solutions(128.7 mM potassium methanesulphonate, 5.1 mM magnesium methanesulphonate, 4.2 mM ATP, 2.0 mM EGTA, 20 mM PIPES, pH 7.0). This pre-activation solutions was replaced for three times and then the solutions in which the small bundle of muscle fibres was immersed was replaced with the activation solutions(84.7 mM potassium methanesulphonate, 5.0 mM magnesium methanesulphonate, 4.3 mM ATP, 10 mM EGTA, 9.99 mM calcium methanesulphonate (pCa 4.4), 20 mM PIPES, pH 7.0).

Tension development was recorded on a pen recorder. The change of resistance of tension gauge(AE801, Akers) was measured. An quick-freeze apparatus (RF10A, Eiko Engineering) (Figure 2) was modified from. When the tension reached a maximum level, the specimen was inserted into the freezing apparatus and the tension level was continuously recorded. The specimen was then rapidly frozen by slamming against a copper block cooled with liquid helium. Then the bundles were frozen in 20 msec (cooling rate: over 10^4 K/sec). The surface of copper blocks was polished with 1 μm diameter diamond compounds and 0.05 μm alumina(Buehler LTD) by polishing machine (ECOMET I, Buehler LTD) and chemically polished by HAYABRIGHT(PHB-D325, Sanhayato). After polishing, the metal block was washed with RDW and with ethanol.

Liquid helium was transferred from the vessel to a quick-freeze apparatus by transfer tube until the copper block was completely immersed. With one transfer, about five bundles of muscle fibres could be quickly frozen. For an experiment, usually the transfer was done three times and the amount of liquid helium needed was about 10 l. Then prepared specimens on sample holders are placed on a plunger(Figure 3), and after removing excess water by pieces of filter paper, the specimens were collided to cooled copper block to freeze rapidly. The frozen specimens were quickly transferred to liquid nitrogen. These specimens were stored in liquid nitrogen. In a month, freeze-substitution was carried out.

The frozen specimens in liquid nitrogen were put in the 2% OsO_4 in acetone solution which was cooled close to the solidification temperature by liquid nitrogen. These solutions were preserved at about -78 °C by keeping the bottles in acetone solutions cooled by solid carbon dioxide for 2 days. After that, the bottles were heated gradually to the room temperature. The bottles were kept at -20 °C, 4 °C and room temperatures for 120 minutes, 60 minutes and 30 minutes, respectively.

The specimens were removed from sample holders and washed with acetone for three times. The tissues were trimmed in acetone. Then the specimens were washed with ethanol for three times. (In each of steps, the specimens was immersed in solutions for 2 or 3 minutes.) The specimens were preserved in 3% OsO_4 in ethanol solutions for block staining for a hour. After staining, the specimens were washed with ethanol for three times. Each of steps took five minutes. The specimens were rinsed with 3 changes of propylene oxide for five minutes each. Tissue blocks were immersed in epoxy resin dissolved in propylene oxide solutions over night (A. Ichikawa *et al.*, 1989).

2.3 Embedding and Thin-Sectioning of Muscle Fibres

The epoxy resin was made from solution A and solution B. The solution A included DDSA 100 ml and Poly/BED 812(Polysciences) 62 ml. The solution B included MNA 89 ml and Poly/BED 812 100 ml. To the mixture of solution A and solution B of the ratio of 5:5–4:6, DMP-30(TAAB) was added up to 1.5%. When the ratio of solution A to solution B was 5:5, the resultant resin was soft and when the ratio was 4:6, the resin was hard. The tissues were immersed in the epoxy resin and were placed in vacuum by pumping by flow of water for two or three hours to remove the water in the epoxy resin. Then the specimens were placed in the oven at 60 °C for about 24 hours and the resin was polymerized. Then the tissues were cooled to the room temperature and stored in a desiccator.

Usually before making ultra-thin sections, semi-thin sections were cut by glass knives to obtain the sections for light microscopy. After light microscopy, I can determine the area for ultra-thin sections. For the staining for light microscopy 1% toluidine blue and 1% sodium tetraborate solutions were used. In this case, the thickness of sections is about 0.35 μm. Then the tissues were trimmed to the cube of 1 cm square by a cutting wheel and ultra-thin sections were made with an ultra-microtome(Ultracut E, Reichelt-Jung). The cutting speed was 1 mm/s and the angle of knife is 45 °. By using diamond knife(Diatome), ultra-thin sections of 40-50 nm thickness were obtained. It was found that hardness of epoxy resin is important to obtain ultra-thin sections. The thickness of the ultra-thin sections were judged from colours of sections. The sections were the shape of trapezoid with shorter edge facing the knife and they are dipped up from water surface with a copper grid.

The grids with collodion membrane were reinforced by evaporation of carbon. Collodion was dissolved by isoamyl acetate before use. The grids were glow-discharged to make the surface hydrophilic and soon they were used to pick up the sections. Continuous ribbons of sections were obtained on water in knife boat so I could mount 5-6 sections on grids without folds. Then the grids were dried on filter paper and the sections were mounted firmly on the grids. These processes of specimen preparation were schematically drawn in Figure 4.

2.4 Staining and Marking with Colloidal Gold Particles

The sections picked up were post-stained for improving the contrast of the images. At first, the grids with sections were put on a drop of the mixture of 3% uranyl acetate solution and ethanol. The staining time to 2 minutes or 4 minutes for transverse sections or longitudinal sections, respectively. The sections were washed by RDW for 30 seconds. And the sections were stained on the grid with lead citrate(Reynolds,). 226 mg lead citrate and 352 mg sodium citrate dihydrate were mixed vigorously in 6 ml RDW for a minute. After 30 minutes of mixing, 1.6 ml of 1N NaOH was added. The staining solution were filled up to 10 ml by RDW. Then I used this Reynolds solution for lead staining. The sections were immersed in the Reynolds solution for 30 seconds. This was done in the absence of carbon dioxide gas, which was removed by grains of NaOH in laboratory dish. After this, the grids with sections were washed with RDW for 1 minutes and dried on a piece of filter paper.

Colloidal gold particles were used as fiducial markers (Luther,P.K., 1988). The solution of colloidal gold particles of 5 nm(Amersham, Japan) were centrifuged at 4800×g for 20 minutes at 4 °C to remove the condensed particles and the supernatants was used. The grids with the sections were floated on a drop of the solution of 5 nm colloidal gold particles for 30 seconds at 4°C with the surface of a carbon film down. Unless this procedure was done before staining, the stain was bleached out during the addition of colloidal gold solution.

2.5 Electron Microscopy of Tilt Series

Sections were examined in a JEM-2000EX(JEOL) electron microscope. The images were recorded with imaging plates or films(FG, Fuji Film and MEM, Mitsubishi). The accelerating voltage was 200 kV. The direct magnification of 50,000 was selected for recording by IP. Minimal dose method was used (R. C. Williams & H. W. Fisher, 1970) and the electron dose for a photograph was about 1 $e/\text{Å}^2$. This very low electron dose was accomplished by the PIXsysTEM(JEOL) (see Appendix A).

The PIXsysTEM uses Imaging Plate (IP) (Figure 6 as a image recording media (Mori,N., et al., 1988). The IP is commercially supplied by Fuji Photo Film Co., type DL-UR$_I$II. Exposed IP was read by IP reader(Fuji DL2000)

with high resolution mode with the pixel size of 50 x 50 μm^2 and sensitivity was set to 50. Image data were stored on a hard disk of a workstation (HEWLETT PACKARD Apollo Series 400).

Using these IP, I took tilt series of the same region of muscle fibres. As tilting angles, I chose 0°, ±15°, ±30°, ±45°, and ±60° with two tilting axes, which are perpendicular to each other. This means that I took 17 photographs from the same region of the muscle fibres. Thus, the total electron dose was reduced to under 20 $e/\text{Å}^2$. In each photograph, an upper limit of defocus contained is 2.0 μm and all micrographs used are in an underfocused range.

After taking this tilt series, I took the photograph of non-tilt specimen to evaluate damages by electron radiation. This photograph compared with the first photograph of a tilt series to determine the resolution of the last photograph. From the comparison of these two photographs, the radiation damage of a section could be estimated.

2.6 Image Processing for Three-Dimensional Reconstruction

Image Processing was carried out as described in Figure 14 on a workstation (HEWLETT PACKARD Apollo DN5500vs). At first, the raw images from PIXsysTEM, which is 2048×1536 pixels large, were converted to represent number of electrons in each pixel for image processing. Then from the images of the standard format, the position of colloidal gold particles was selected. Assuming the density of gold particles is much larger than that of background, the centre of mass of the particle is calculated from the densities of pixels of the selected region.

Next, using initial angles of planes of the tilted sections, the three-dimensional coordinates of markers were calculated and corrected by the least-square technique (Luther,P.K., 1988). The deviation of the projected coordinates of the markers was minimized by direction set (Powell's) method (Press,W.H., 1992). The Eulerian angles, ϕ, θ, and ψ for rotation, and a scaling factor m were defined as:

$$\begin{pmatrix} x'_o(i) \\ y'_o(i) \\ z'_o(i) \end{pmatrix} = \begin{pmatrix} \cos\psi & \sin\psi & 0 \\ -\sin\psi & \cos\psi & 0 \\ 0 & 0 & 1 \end{pmatrix} \begin{pmatrix} 1 & 0 & 0 \\ 0 & \cos\theta & \sin\theta \\ 0 & -\sin\theta & \cos\theta \end{pmatrix} \begin{pmatrix} \cos\phi & \sin\phi & 0 \\ -\sin\phi & \cos\phi & 0 \\ 0 & 0 & 1 \end{pmatrix}$$

$$\times \begin{pmatrix} m & 0 & 0 \\ 0 & m & 0 \\ 0 & 0 & 1 \end{pmatrix} \begin{pmatrix} x_o(i) \\ y_o(i) \\ z_o(i) \end{pmatrix}$$

where $x_o(i)$, $y_o(i)$, and $z_o(i)$ are measured coordinates of fudicial markers in the ith plane. Then the differences between the rotated coordinates, $x'_o(i)$, $y'_o(i)$, and $z'_o(i)$, and the reference coordinates, $x_o(0)$, $y_o(0)$, and $z_o(0)$, were squared and summed up as:

$$S = \sum_{i\neq 0}((x'_o(i) - x_o(0))^2 + (y'_o(i) - y_o(0))^2 + (z'_o(i) - z_o(0))^2)$$

where the plane of $i = 0$ is the one without rotation. This value S is minimized iteratively by Powell's method. The used markers are from 5 to 8 and the centre of mass of these markers are assumed to be at the origin.

Then I could correlate the corresponding points on each of sections from the corrected angles of tilted sections. I selected a region for three-dimensional reconstruction on a non-tilted view, because I can see thin and thick filaments most clearly in that view. Thus I could calculate the coordinates of the corresponding regions in sections and cut out the region from the images of tilt series after the bicubic spline interpolation in two dimension. The resulting images were 128×128 pixels large.

I next made a histogram of the images by separating their values of density into about 60 classes from the maximum value to the minimum value. The number of classes was changed depending the shape of resulting histograms. Then I modelled the histogram by adding two Gaussian curves;

$$a_1 e^{-\frac{1}{2}(\frac{x-m_1}{d_1})^2} + a_2 e^{-\frac{1}{2}(\frac{x-m_2}{d_2})^2}.$$

By assuming m_1 and m_2 are the average of densities from background and proteins respectively, I multiply the densities of each image by a constant so that $m_1 = 0$ and $m_2 = 1$. Note that usually the electron densities of pixels which represent proteins are smaller than the ones of background, thus the brightness of images was reversed. By this process, I could unify the densities of tilt series. Since tilted sections are thicker than the non-tilted ones along an electron beam axis, they should be darker. To accommodate this factor, the densities of images were multiplied by the factor for correction relating with the Eulerian angles of planes of tilted sections.

2.7 Three-Dimensional Reconstruction Techniques

Here I obtained the final normalized data set of tilt series of the same region of sections of muscle fibres. Then I simply back-projected the images into three-dimensional space: The projections are smeared out to form so called back-projection bodies and all the back-projection bodies are summed up. Then I could make the three-dimensionally reconstructed image of $128 \times 128 \times 128$ pixels large. (See Appendix B.)

To determine the resolution of the reconstructed image, I calculated the value using the observed electron densities f_o and the calculated densities of an object f_c;

$$ r = \frac{\sum_{\text{all pixels}} |f_o - f_c|}{\sum_{\text{all pixels}} f_o}. $$

This value is close related to the R value (Blundell,T.L. & Johnson,L.N., 1976), which is used in X-ray crystallography, but r is calculated in the real space. In X-ray crystallography, values are measured in the Fourier space, while in this case the observed electron dose is in the real space. Therefore, it is natural to compare the differences in the real space, although in the real space, it is difficult to discuss about resolutions of reconstructed images.

To consider about the resolution of the reconstructed image, low-pass filtering was used. Each observed images and the projected images from the reconstructed image were averaged into various pixel size; 2, 4, 8, 16 nm. By comparing r value described above, I can speculate the reasonable resolution of the reconstruction. By comparing r value of each measured image, which is taken one by one, I can also consider the effect of radiation damage.

From this analysis, I can determine the resolution of the reconstructed image. Next, to increase signal-to-noise ratio, I filtered the reconstructed image by substituting the pixel values with the median of the surrounding pixels. For the area of substitution, I choose the cubic with the radius of resolution I determined as above. Then I displayed the stereo view of the median-filtered reconstructed images to grasp the position and the shape of cross-bridges in contracting muscle fibres. The surface of cross-bridges was determined so that thick filaments could be traced continuously. In Figure 14, an overview of the process of image analysis for three-dimensional reconstruction was shown.

14

3 Results

3.1 Electron Micrographs of Contracting Muscle Fibres

The low magnification image of a cross-section of rapidly-frozen muscle fibres during isometric contraction is shown in Figure 9. The arrows are representing the contact surface of muscle fibre to a cooled copper block, and muscle fibres are observed under the surface. The upper region of the muscle fibre is preserved better than the lower region, because the filaments are circular with uniform diameter. In deeper region, the filaments of uniform diameter cannot be observed. Thus, it is easy to search the contact region in specimen. From this figure, it is estimated that the well-preserved region is 1 μm deep. I, therefore, used the region that is under 1 μm from the interface for image analysis below.

Figure 10 shows electron photographs in rigor, relaxed, and contracting states taken using films with the electron dose of about 10 $e/\text{Å}^2$. Thus, in this figure, thin filaments and cross-bridges attached to them are clearly observed, while thick filaments are also clearly seen. In rigor and contracting states, the diameters of thick and thin filaments resemble. On the other hand, in relaxed state the thick filaments are thicker, while the thin filaments are thinner. The background between thin and thick filaments in relaxed state is clear with little cross-bridges attached to thin filaments.

Next, I show a middle-magnification image of a cross-section of rapidly-frozen specimen in Figure 11 with the upper-right inset of its magnified image. Because this photograph was taken using IP with low electron dosage, the figure is noisy. In the inset of this figure, thick filaments aligned on a hexagonal lattice are observable, while it is difficult to see thin filaments clearly because of low signal-to-noise ratio. The low signal-to-noise ratio is due to the very low electron dose (1 $e/\text{Å}^2$), essential for taking many photographs of the same region. There are faintly bright spots between the thick filaments. These faint glints represent thin filaments.

In this middle-magnification image, one can see small white particles scattered all over the images. These are colloidal gold particles attached to sections as fiducial markers before post-staining of sections. This distinguishable mass of colloidal gold particles could distort the three-dimensional image. Thus, I excluded the region with these spots from the reconstruction. So these parti-

15

cles are used for calculation of Eulerian angles and scaling factors. They are also used for justification of three-dimensional reconstruction. Their signal is very strong and noise contribution to reconstructed images could be neglected. The cubic reconstructed image of colloidal gold particles could be obtained.

In Figure 12, I show the tilt-series of electron micrographs from the same region of a muscle fibre. In Figure12 (a), the non-tilted image is shown. The 15°, 30°, 45°, and 60°-tilted image are shown Figure 12 (b), (c), (d), and (e), respectively. From the positions of colloidal gold particles, the relative tilt angles of sections could be estimated. In Figure 12 (e), the degree of defocus changes rapidly from left to right. One can see this effect from the fringe of white spots that represent colloidal gold particles. When the particles are in underfocus region,they have darker fringe. In upperfocus region, the contrast of particles is reversed. The left part of this image is near zero defocus than the right part but even the most-right portion is underfocused. I used only the photographs with underfocus for image analysis and estimated defocus of the photographs is about 1 μm. Thus the defocus of electron micrographs cannot limit the resolution of images.

3.2   Correction of Plane Angles of Tilted Thin Sections

To determine plane angles of sections, I first measured coordinates of colloidal gold particles. Next, by minimizing deviations between calculated positions and measured positions of colloidal gold particles, I corrected the Eulerian angles and scaling factors of sections (Section 2.6). The corrected values of the Eulerian angles and scaling factors are shown in Table 1. In Table 1, I listed all the corrected Eulerian angles of planes against non-tilted views. From these data, one can see the difference between the measured angles from goniometer and the calculated angles by minimization. This is because tilting axis of goniometer was not perfectly perpendicular to projection axis. Thus this process of correction is essential for precise alignment of sections.

In Table 2 (a), I listed the projected two-dimensional measured and corrected coordinates of colloidal gold particles on each image of tilt-series. The correction was done from the estimated three-dimensional coordinates of colloidal gold particles using the corrected Eulerian angles. The deviations between the two coordinates are under 2 pixel, which is 2 nm. These deviations are mainly caused by noises on images and actual movement of colloidal gold particles because of non-uniform deformation of sections by electron radiation.

16

Thus I consider the estimated three-dimensional coordinates of colloidal gold particles is determined within 2 nm resolution in the non-tilted view. Because sections cannot be projected with the tilting angle over 60°, some region in Fourier space cannot be obtained the transforms. This region is called a missing region (Radermacher,M., 1992). Because of this missing region, the accuracy of the estimated three-dimensional coordinates differs in x-y plane and in z-direction.

To estimate error in z-direction, I assume the surface of the section is flat and colloidal gold particles are attached to the surface. On this assumption, the distances from the colloidal gold particles to the surface of a section were calculated. They are tabulated in Table 2 (b). As one can see in this table, the errors in z-direction is within 3 pixel. So the estimation of coordinates in z-direction is better than 3 nm. I, therefore, can consider that coordinates in z-direction is also well determined, although the missing rigion causes slightly worse result of estimated errors of coordinates in z direction than in x-y direction. The estimated coordinates of colloidal gold particles in z-direction show that the section is not exactly aligned perpendicular to the electron beam axis in the non-tilted image. The tilted angle of the electron beam axis to the section, however, is below 2°. So this tilt doesn't affect the defocus of images significantly.

Also these deviations of measured positions of colloidal gold particles don't limit the resolution of the reconstructed images because the estimated resolution of the reconstructed images are about 4-8 nm (Section 3.4).

3.3   Normalization of Electron Densities

Two Gaussian curves, which represent electron densities from background and proteins, are fitted to electron densities of images. The difference between two Gaussian curves is due to the difference between densities of background come from resin and that of proteins come from staining agents. The electron densities of different materials have the different distribution of densities.

The Figure 15 shows examples of the histogram of electron densities in each pixel of a non-tilted view and a 60°-tilted view. In Figure 15 (a), the histogram of a non-tilted image was shown. The measured data were displayed by square dots and the fitted data of addition of two Gaussian curves was drawn by a broken line. There is no significant difference between the measured data and the fitted data. Also in Figure 15 (b), I show the histogram of a 60°-tilted

17

view. In this graph, there is no significant difference.

To confirm the assumption that two Gaussian curves come from electron densities of proteins and resin, the upper and lower cutoff levels of the image were changed to correspond two Gaussian curves. In Figure 16 (a), the cutoff level of the densities of the image was set to be $m_1 \pm d_1$, respectively. Densities representing background are graded, while densities representing proteins are uniformly black. On the other hand, the cutout levels were set to be $m_2 \pm d_2$ (Figure 16 (b)). The pixels displayed with gray levels are corresponding to proteins, and background is uniformly white. From this figure, it is concluded that two Gaussian curves represent background and proteins.

Using these obtained data, I normalized the images cut out from the original image. An example of normalized images I used for three-dimensional reconstruction was shown in Figure 17. In this figure, the cutoff levels of images were set to be $m_1 \pm (m_2 - m_1)$. In this figure, the cutoff levels are so close that the magnified images look noisy. This means low signal-to-noise ratio of the original images, although by averaging the images of various tilting angles will improve the signal-to-noise ratio.

3.4 Three-Dimensional Image Reconstruction by Simple Back-Projection

At first, the point-spread function of the geometry of this experiment was calculated (data not shown). By this calculation, it was shown that the missing region caused the smearing effect into z-direction. This smearing was within a pixel when the signal-to-noise ratio of the image was 1. Next, I reconstructed a colloidal gold particle by simple back-projection method (data not shown). The reconstructed images of the colloidal gold particle with diameter of 10 nm were circular and no significant deformation cannot be observed. The improvement of signal-to-noise ratio by averaging images could not be measured, because high signal-to-noise ratio of the original image of colloidal gold particles was high enough. Thus the improvement was estimated in the reconstructed image of filaments of muscle fibres.

In Figure 18, the three-dimensional image reconstructed by simple back-projection method is shown. These are 6 slices of the reconstructed images that are perpendicular to a z-axis. The hexagonal lattice of thick filaments can be seen, while it is difficult to distinguish thin filaments and cross-bridges from background because of low signal-to-noise ratio. Comparison of these slices with the original observed images (Figure 17) shows that the signal-to-noise ratio is improved.

To estimate the resolution of the reconstructed images, I calculate the r value between the projected images from the reconstructed image and the observed images. In Figure 20, the calculated r values at various resolutions are shown. The assumed resolutions are 1, 2, 4, and 8 nm and the r values decrease and converge to a finite value. From the shape of this decreasing curve, I estimated the resolution of this reconstructed image used in this calculation is between 4 and 8 nm. Other reconstructed images also gave the similar result.

Using this r value, I also estimated the damage by electron radiation. For this purpose, I compared the observed images taken one by one to the projected images from the reconstructed image. If the damage of radiation is critical, the r values will decrease during taking tilt series. Figure 19 shows the result of this analysis. No correlation between accumulated electron dose and the r values was not observed. It means that significant damage by electron radiation was not observed at this resolution.

To improve this low signal-to-noise ratio, I use median filtering technique. I replaced pixel values with the median of pixel values in a cube of 4 pixel radius. By this processing, I could reduce white noises. Thus, I could produce a contour map of slices of the three-dimensional image. From the contour map, the surface of proteins was determined, and the stereo views of filaments were produced. An example of the stereo views is displayed in Figure 21. Because the reasonable contour map can be produced by the median filtering of pixel in a cube with a radius of 4 nm, the resolution of this reconstructed image may be considered 4-8 nm or less. This well matches with the analysis of r value.

3.5 Characteristic Features of Thick Filaments in Contracting Muscle Fibres

In Figure 21, a shaded view of the contracting muscle fibres, which was seen from the direction of M-line, were displayed. In this figure, hexagonal lattice of thick filaments can be clearly seen, although thin filaments cannot be identified as the continuous filaments: thin filaments are observed only when cross-bridges are attached to them. The thick filaments are represented by black circles in Figure 21 and the thin filaments are designated by white circles. Thus

I could isolate each thick filament and cross-bridges from this reconstructed data by removing far region of the thick filament. The side views of extracted thick filaments was displayed in Figure 22.

In these side views of thick filaments, the density of cross-bridges is high and they are observed clearly. The direction of M-line is considered upward, because many cross-bridges are pointing upward in this section of contracting muscle fibres. From the longitudinal sections of contracting muscle fibres, a lot of cross-bridges are pointing to the direction of M-line (Funatsu,T., *et al.*, 1993).

Also in this figure, the 14.3 nm pitch of myosin heads on thick filaments can be recognized. this pitch corresponds to the spot of the diffraction pattern observed by X-ray experiments of contracting muscle fibres, and the spot is also observed in computed diffraction pattern of longitudinal sections. The estimated point of myosin heads are pointed by arrows. The rotation of cross-bridges along the thick filament displayed in the schematic drawing in Figure 23 also was observed. Thus the possibility that this feature is the artifact of three-dimensional reconstruction is very low, because the two axes of tilting are perpendicular and it is difficult to show the 120° rotation of cross-bridges.

3.6 Characteristic Shapes of Cross-bridges in Contracting Muscle Fibres

As seen in Figure 22, there are many types of cross-bridges and their shapes vary from one another. In these various shapes of cross-bridges, I have shown a typical type of cross-bridges in the reconstructed images in Figure 23. This is the 'tadpole'-like cross-bridge, similar to the cross-bridge in muscle fibres in rigor state. This cross-bridge seems to have two myosin heads in these densities from the estimation of thickness of the cross-bridge. The width and thickness of myosin S1 is 65 Å and 40 Å, respectively (Rayment,I., *et al.*, 1993(a)).

Another type of cross-bridges different to the 'tadpole'-like cross-bridges is shown in Figure 24 and designated by an arrowhead. From the volume of this cross-bridge, it seems to contain only one myosin head in it. In Figure 22, there are many types of cross-bridges which are represented by arrowheads and they can't be divided into several typical types of cross-bridges. These various shapes of cross-bridges may mean that the cross-bridges in contracting muscle fibres are very flexible.

20

Another type of myosin heads is positioned in the very close region of a thick filament. This type of myosin heads is shown in Figure 24 and represented by an arrow. When myosin heads are not attached to thin filaments, the thick filaments are thicker than other regions. This means that myosin heads are near the thick filament and the densities of the myosin heads make the thick filament thicker. This explains that thick filaments are thicker in relaxed state than in rigor and contracting state (Figure 10). In relaxed state, most myosin heads are near thick filaments and therefore thick filaments look thicker.

3.7 Number and Orientation of Cross-bridges Attached to Thin Filaments

To estimate the fraction of cross-bridges attached to thin filaments in isometric contraction, I counted the number of cross-bridges protruding to thin filaments. Because the thickness of the section is about 40 nm and the pitch of myosin head is about 14.3 nm, 2 positions on a thick filament are considered to the region where myosin heads are present. Since three myosin molecules are thought to be present in a region of thick filaments (Figure 23, 6 myosin molecules are present in a thick filament of the reconstructed data.

Thus, among 36 positions where myosin heads must be present from 6 thick filaments (Figure 22), 14 cross-bridges could be observed. From this estimation, the number of cross-bridges bound to thin filaments are calculated to be about 40% of the total myosin molecule. Since a myosin molecule has two heads in it, the portion of myosin heads binding to thin filaments can be estimated from 20% to 40%. Actually, the observed cross-bridges could be divided into two types: one myosin head containing (Figure 23) and two myosin heads containing (Figure 24) cross-bridges, as described in Section 3.6. Assuming two myosin heads observed in a cross-bridge are both attached to a thin filament, the portion of cross-bridges attached to thin filaments is about 35%, because the number of one-myosin-head-containing cross-bridge is 3 in 14 observed cross-bridges.

It is difficult to estimate orientation of cross-bridges, because the shape of cross-bridges varies one another. At least, thin filaments with many cross-bridges attached to themselves could not be observed. This means that the cross-bridges are sticking out from thick filaments randomly without preferred thin filaments. Actually, they are protruding along the symmetry of thick fil-

21

aments (Figure 22). About the lateral angle of cross-bridges to the attached thin filament, many cross-bridges are tilted upward in this figure. So I determined the M-line is in the upward direction of this figure and other figures (Figure 23, 24).

4 Discussion

4.1 Used Regions for the Three-Dimensional Reconstruction

I used the region of the rapidly-frozen muscle fibres in 1 μm from the surface. Because the freezing of a muscle fibre starts from the region that contacted to the cooled copper block, well-preserved area of the muscle fibre is confined to the region near the interface to water. By limiting a region for reconstruction to this area, I could observe clear lattice of filaments. Hexagonal lattice of filaments, however, are a little warped in the region near the contacted surface because of the smashing pressure by the contact to a copper block. Other groups reported much deeper region of preservation about 10 μm.(Tsukita, S. and Yano, M., 1985; Usukura,J. *et al.*, 1983). In my experiments, some samples were well-preserved within the region of about 10 μm deep, too. When I compared these well-preserved region of muscle fibres, no difference of the structure could be observed. I, therefore, used both regions assuming they are same.

As written above, the smashing to a cooled copper block causes deformation of hexagonal lattice of filaments. This effect was avoided by excluding deformed region near the contact surface of the muscle fibre. Another candidate for deformation of hexagonal lattice is non-uniform contraction. Contraction of muscle fibres may not be started uniformly in a muscle fibre, because I initiated contraction by diffusion of Ca^{2+} ions. This effect can be seen by the lateral alignment of Z-lines, typically better with the photolysis technique of caged-ATP than by this solution exchange (K. Hirose *et al*, 1993; T. Funatsu *et al*, 1993). Muscle fibres, however, contracted uniformly, as they were rapidly frozen, because I waited until the state of isometric contraction was achieved. Also, the region of observation is localized near the surface of solution exchange. Therefore, in this region, the uniform contraction can occur.

4.2 Necessity of Normalization from the Data of the Images

The conditions of area in which I took electron micrographs differ from picture to picture, because I use the same region of a section for electron microscopy.

The "clearing" effect of a section occurs at the first or the second radiation of electrons. Also the section was contaminated at each electron radiation (Luther,P.K., *et al.*, 1988). Section collapse and planar shrinkage were measured, too. In the electron dose of this experiment, the collapse and shrinkage of the section are not significant. On the other hand, the "clearing" effect was observed, when the electron dose is 0.1 e/Å². Thus this effect cannot be neglected, and the normalization from the data of each photograph is necessary.

I multiplied the unified densities of each photograph by $\cos\theta$ (Section 2.6). This means that the normalization of electron dose was carried out assuming the uniform distribution of proteins in a section. This may be wrong because the proteins in sections have filamentous features and they place in lattice. However, there are enough densities between filaments to assume the uniform distribution of densities of proteins. Actually, the reconstructed images of proteins were clearly seen after the normalization by this technique.

4.3   Weighted Back-Projection of Images with Low Signal-to-Noise Ratio

I tried weighted back-projection to reconstruct three-dimensional images, because the simple back-projection calculates only an approximation of the object. In weighted back-projection method, weighting function, was multiplied to the Fourier transform of the reconstructed image by simple back-projection method. The weighting function can be calculated from the geometry of each section (Appendix B). Thus the true densities of muscle fibres can be deconvoluted.

The calculated three-dimensional image of contracting muscle fibres by weighted back-projection, however, was noisier than that obtained by simple back-projection. Because of the limited number of projections and their low signal-to-noise ratio,strange patterns depending on the geometry of projection appeared due to noise of the data. These patterns are not rapidly changed in the reconstructed images but globally changed. Thus these patterns could not be eliminated by median filtering and it was difficult to determine a single contour level to display continuous filaments. These patterns occurred because densities of a section of finite thickness smeared in z-direction by the effect of missing cone. So the densities are more dense in the center of a section than the surface of the section.

Also the reconstruction of cross-bridges was carried out in Fourier space. The Fourier transforms of each image are corresponding sections of the three-dimensional Fourier transforms of the three-dimensional image. Thus the reconstructed image are calculated by inverse Fourier transformation of interpolated Fourier transforms of observed images. The interpolation of Fourier transforms, however, is time-consuming, and there is no advantage of calculating Fourier transforms, because no noise is reduced in Fourier space. Thus, it was difficult to reconstruct big three-dimensional images like $128 \times 128 \times 128$ pixels, and the reconstruction was carried out in real space.

4.4   Resolution of the Reconstructed Images

The analysis of resolution of the reconstructed images was done in real space. This is because the observed values are data in real space, while in X-ray crystallography, for instance, the measured values are data in Fourier space. The calculation of r value in real space is almost same as R value in Fourier space. Only positive values are used in the calculation of R value in Fourier space because amplitudes must be positive. In real space, also pixel values of the observed images must be positive, therefore it is similar to the situation of calculation of R value.

This requirement of positive values is why I used averaged images to compare images at various resolution rather than low-passed images. The simple low-passed images may have negative values and these negative values complicate the interpretation of r value. Maybe I can use low-passed images with weights of Gaussian distribution to conserve the positiveness of data. In the situation of only positive values, the calculated r value converged to a finite value (Figure 20).

From the convergence of r value, I estimated the resolution of the reconstructed images. The estimated resolution is from 4 to 8 nm, at which the r value converged to almost the finite value. At this resolution, signal and noise are distinguished and signals were cancelled in calculated and observed images. By the analysis in Fourier space, the similar estimation of resolution could be derived, although the behavior of R value in Fourier space was complicated. This is because densities of proteins in muscle fibres are distributed without boundaries.

At the resolution of 4-8 nm, it was difficult to observe thin filaments clearly because the maximum diameter of F-actin is between 90-95Å(Holmes,K.C.,

1990). Although thin filaments are decorated by various actin binding proteins like tropomyosin and troponin, this maximum diameter of F-actin is approximately the maximum diameter of thin filaments. On the other hand, both thick filaments with diameter of about over 10 nm and myosin S1 with the length of about 16 nm (Rayment,I., *et al.*, 1993(a)) were observed.

4.5 Number of Cross-bridges Bound to a Thin Filament

Assuming the 14.3-nm periodicity of myosin heads, almost same volume of myosin heads could be seen on thick filaments. This means that all myosin heads are observed in this three-dimensional reconstruction. Thus, by classifying these densities into actin-attached myosin heads and free myosin heads that are near thick filaments, the number of cross-bridges bound to a thin filament can be estimated. The estimated ratio of myosin molecules bound to thin filaments divided by the number of myosin molecules was about 1/3. Thus 1/3 - 1/6 of myosin heads are bound to thin filaments, considering two heads of a myosin molecule.

This number agrees with the model of muscle contraction (Huxley, A.F., 1957) but it may conflict with the X-ray diffraction studies (Haselgrove & Huxley, 1973; Matsubara *et al.*, 1975) and stiffness measurements (Goldman & Simmons, 1977) of frog muscle suggested that 50-90% as many heads are attached during contraction. This may be explained by assuming only binding myosin molecules are detected by this three-dimensional reconstruction, while X-ray diffraction studies may detect myosin molecules that are positioned only near thin filaments. Only myosin molecules bound to thin filaments may be cross-linked to thick filaments in freeze-substitution technique.

4.6 Characteristics of Structure of Cross-bridges in Muscle Fibres

Many reports showed that myosin heads are angled when they bind to actin filaments in the rigor state (Huxley, H.E., 1963; Reedy,M.K., *et al.*, 1965). In the three-dimensional reconstruction of actin filaments decorated by myosin S1, the angle of S1 was close to 90° to the filament axis in the region near the thin filament and smaller than 45° in the tail region (Toyoshima & Wak-

abayashi, 1985; Milligan & Flicker, 1987). Also in muscle fibres, the structure of cross-bridges in rigor state were examined in three-dimensional reconstruction (Taylor,K.A., *et al.*, 1989). In muscle fibres, cross-bridges in rigor state have two characteristic types of structure that are distinguished by the number of myosin S1 contained in them. Two myosin heads in a cross-bridges were not distinguished clearly.

These features can be seen in the cross-bridge indicated by the arrowhead in Figure 23, although there is other types of cross-bridges observed in reconstructed images of contracting muscle fibres like in Figure 24. This agrees with variable angles of cross-bridges in fibres that still prefer angles close to 45° (Trombitás,K., *et al.*, 1986; Heuser,J.E., 1987; Taylor,K.A., *et al.*, 1989). This result indicates that rigor state should exist in the ATPase cycle of active state. This implication agrees with the proposed model from the molecular basis of muscle contraction. In this model, the spatial relation between the ATP binding pocket and the major contact area on actin suggests a working hypothesis for the cross-bridge cycle (Rayment,I., *et al.*, 1993).

I described two typical types of cross-bridges in the result (Section 3.6), while I could observe many other cross-bridges in the reconstructed image of muscle fibres. From these observations, I think that it is difficult to classify these cross-bridges into several types. They are distributed continuously over a possible range from consideration of many types of the structure. This wide variety of types of myosin cross-bridge structure may be important for myosin molecules to change chemical energy of ATP into mechanical energy.

Acknowledgement

28

References

1. Bagshaw, C.R. 1982. Muscle Contraction. Chapman and Hall Ltd, London. 1 pp.

2. Blundell, T.L. and L.N. Johnson. 1976. Protein Crystallography. Academic Press Inc., San Diego, CA.

3. Cooke, R., M.S. Crowder, and D.D. Thomas. 1982. Orientation of spin labels attached to cross-bridges in contracting muscle fibres. *Nature* **300**:776-778.

4. Eisenberg, E. and T.L. HIll. 1985. Muscle contraction and free energy transduction in biological systems. *Science* **227**:999-1006.

5. Funatsu, T., E. Kono, and S. Tsukita. 1993. Time-resolved Electron Microscopic Analysis of the Behavior of Myosin Heads on Actin Filaments after Photolysis of Caged ATP. *J. Cell Biol.* **121**:1053-1064.

6. Harada, Y., K. Sakurada, T. Aoki, D.D. Thomas, and T. Yanagida. 1992. Mechanochemical Coupling in Actomyosin Energy Transduction Studied by in Vitro Movement Assay. *J. Mol. Biol.* **216**:49-68.

7. Heuser, J.E., T.S. Reese, M.J. Dennis, Y. Jan, L. Jan, and L. Evans. 1979. Synaptic vesicle exocytosis captured by quick freezing and correlated with quantal transmitter release. *J. Cell Biol.* bf 81:275-300.

8. Higuchi, H. and Y.E. Goldman. 1991. Sliding distance between actin and myosin filaments per ATP molecule hydrolysed in skinned muscle fibres. *Nature* **352**:352-354.

9. Hirose, K. and T. Wakabayashi. 1993. Structural change of cross-bridges of rabbit skeletal muscle during isometric contraction. *J. Musc. Res. Cell Motil.* **14**:432-445.

10. Huxley, A.F. 1957. Muscle Structure and Theories of Contraction. *Prog. Biophys. Biophys. Chem.* **7**:255-318.

11. Huxley, A.F. and R. Niedergerke. 1954. Structural Changes in Muscle during Contractin. *Nature* **173**:971-973.

29

12. Huxley, A.F. and R.M. Simmons. 1971. Proposed Mechanism of Force Generation in Striated Muscle. *Nature* **233**:533-538.

13. Huxley, H.E. and J. Hanson. 1954. Changes in the Cross-Striatin of Muscle during Contraction and Stretch and Their Structual Interpretation. *Nature* **173**:973-976.

14. Kabsch, W., H.G. Mannhetz, D. Suck, E.F. Pai, and K.C. Holmes. 1990. Atomic structure of the actin:DNase I complex. *Nature* **347**:37-44.

15. Katayama, E. 1989. The Effects of Various Nucleotides on the Structure of Actin-Attached Myosin Subfragment-1 Studied by Quick-Freeze Deep-Etch Electron Microscopy. *J. Biochem.* **106**:751-770.

16. Luther, P.K., M.C. Lawrence, and R.A. Crowther. 1988. A Method for Monitoring the Collapse of Plastic Sections as a Function of Electron Dose. *Ultramicroscopy* **24**:7-18.

17. Mori, N., T. Oikawa, T. Katoh, J. Miyahara, and Y. Harada. 1988. Application of the "Imaging Plate" to TEM Image Recording. *Ultramicroscopy* **25**:195-202.

18. Radermacher, M. 1992. Weighted Back-Projection Methods. In Electron Tomography. J. Frank, editor. Plenum Publishing Co., 91-115.

19. Rayment, I., H.M. Holden, M. Whittaker, C.B. Yohn, M. Lorenz, K.C. Holmes, and R.A. Milligan. 1993. Structure of the Actin-Myosin Complex and Its Implications for Muscle Contraction. *Nature* **261**:58-65.

20. Rayment, I., W.R. Rypniewski, K. Schmidt-Base, R. Smith, E.R. Tomchick, M.M. Benning, D.A. Winkelmann, G. Wesenberg, and H.M. Holden. 1993. Three-Dimensional Structure of Myosin Subfragment-1: A Molecular Motor. *Science* **261**:50-58.

21. Reynolds, E.S. 1966. The Use of Lead Citrate at High pH as an Electron-opaque Stain in Electron Microscopy. *J. Cell Biol.* **17**:208-213.

22. Taylor, K.A., M.C. Reedy, L. Cordova, and M.K. Reedy. 1989. Three-Dimensional Image Reconstruction of Insect Flight Muscle. I. The Rigor Myac Layer. *J. Cell Biol.* **109**:1085-1102.

23. Toyoshima, C. and T. Wakabayashi. 1979. Three-Dimentional Image Analysis of the Complex of Thin Filaments and Myosin Molecules from Skeletal Muscle. *J. Biochem.* **86**:1887-1890.

24. Toyoshima, C. and T. Wakabayashi. 1985. Three-Dimensional Image Analysis of the Complex of Thin Filaments and Myosin Molecules from Skeletal Muscle. V. Assignment Subfragment-1 Complex. *J. Biochem.* **97**:245-263.

25. Toyoshima, C. and T. Wakabayashi. 1985. Three-Dimensinal Image Analysis of the Complex of Thin Filaments and Myosin Molecules from Skeletal Muscle. IV. Reconstitution from Minimal- and High-Dose Images of the Actin-Tropomyosin-Myosin Subfragment-1 Complex. *J. Biochem.* **97**:219-243.

26. Tsukita, S. and M. Yano. 1985. Actomyosin Structure in Contractin Muscle Detected by Rapid Freezing. *Nature* **317**:182-184.

27. Uyeda, T.Q.P., S.J. Kron, and J.A. Spudich. 1990. Myosin Step Size Estimation From Slow Sliding Movement of Actin Over Low Densities of Heavy Meromyosin. *J. Mol. Biol.* **214**:699-710.

28. Wakabayashi, K., M. Tokunaga, I. Kohno, Y. Sugimoto, T. Hamanaka, Y. Takezawa, T. Wakabayashi, and Y. Amemiya. 1992. Small-Angle Synchrotron X-ray Scattering Reveals Distinct Shape Changes of the Myosin Head During Hydrolysis of ATP. *Science* **258**:443-447.

29. Williams, R.C. and H.W. Fisher. 1970. Electron Microscopy of Tobacco Mosaic Virus under Conditions of Minimal Beam Exposure. *J. Mol. Biol.* **52**:121-123.

30. Yanagida, T. 1981. Angles of Nucleotides Bound to Crossbridges in Glycerinated Muscle Fiber at Various Concentration of e-ATP, e-ADP and e-AMPPNP Detected by Polarized Fluoresence. *J. Mol. Biol.* **146**:539-560.

Appendix

A PIXsysTEM

The IP is mainly made of phosphor, which consists of Ba, F, and halogen $X(X=Cl, Br, I)$ doped with Eu^2+, and can store the energy of incident electrons. When electrons penetrate the phosphor, electron-hole pairs are created,then created electrons are trapped at the defects of crystal of phosphor, and holes are trapped at Eu^2+. In the step of reading out the data of stored energy from the IP, the phosphor is irradiated with visible light (He-Ne laser is used). This light excites the trapped electrons and electrons recombine with the holes. Its recombinationn energy is converted to photons of about 390 nm wavelength at Eu^2+. The photons are guided to a photomultiplier tube and converted to electrical signals there (Mori,N., *el al.*, 1990).

Fundamental characteristics of IP can be summarized into two points (Fig 6).

High Sensitivity the precision of measurement went down below the density of $10^{-12} A/cm^2$.

Good Linearity with Wide Dynamic Range Dynamic range of the data obtained is 4 decades for an image and the response of IP is linear within this range.

From the metal mask of 30 μm thick nickel, the resolution of IP was measured. if we define the resolution as the frequency of response 0.4, the resolution is 77 μm. The IP have its maximum intensity at about 150 kV at the dose of 10^{-11} C/cm^2.

PIXsysTEM is a newly developed "Imaging Plate System for a transmission electron microscope" which is a total system covering processes from image acquisition to image printing (Oikawa,T. *et al.*, 1990). The system is composed of the following five units.

1. Imaging Plate (IP) designed for a TEM

2. IP-camera installed in a TEM

3. IP-reader

4. IP-processor

5. IP-printer

Figure 7 shows a schematic diagram of the PIXsysTEM. An outline of the system along the image data flow is explained below.

The size of the IP is designed to be 102×127 mm with a 0.36 mm thickness. The effective exposure area on the IP is 77×102 mm. Twenty-six IPs accommodated in an IP-magazine and are set into the IP-camera in the TEM. After exposure, the IPs are taken out from the IP-camera, and set into the IP-reader by the operator. On the other hand, when the IP-magazine is set into the TEM, the operator sets a memory card into the memory-card-writer in the TEM. After exposure, the memory card is taken out from the TEM, and set into memory-card-reader in the IP-processor by the operator.

The IP-processor automatically adjusts a reading sensitivity according to the information from the memory card, on the exposure accelerating voltage and electron dose. The reading pixel size is 50×50 μm, and the number of pixel in a single image is 1,536×2,048 (3,150,000 pixels.) The signal intensity read out from the IP is digitized into 4,096 gray levels (12 bits), which corresponds to the range of about 4-order electron dose. The memory size is 6.3 Mbytes (1,536×2,048×2 bytes with a 4 bit blank) for a single image.

After the reading, the IP is irradiated with a sufficient light in the IP-reader. This process erases the image remaining on the IP even after the reading, and makes the IP reusable. To use IP next time, I usually erase the IPs for three minutes with sufficient light irradiation to erase the image data completely within 12 hours before use. The image data with the information is displayed on the monitor CRT and stored on the hard disk in the IP-processor.

B Back-Projection Method

The back-projection or summationtechnique is an intuitively simple reconstuction method. The technique can most easily be explained using the example of a simple two-dimensional binary object consisting, e.g., of three disk-shaped regions with value 1 inside and value 0 outsize. This object is to be reconstructed from its one-dimensional projections (Fig 8). The object O appears in the projection P_1, P_2, P_3, and P_4 at angles θ_1, θ_2, θ_3, and θ_4. As a first step in the reconstuction process, the projections are smeared out to form so

called back-projection bodies. To reconstruct the object, one has to sum all the back-projection bodies.

The simple back-projection calculates only an approximation of the object. To obtain a faithful reconstruction, the back-projected density has to be corrected. This correction can be achieved by the convolution with a function that acts as the inverse of the point-spread function. In weighted back-projection methods this deconvolution is achived by a division of the Fourier transform of the back-projected density by the transfer function of the reconstruction algorithm.
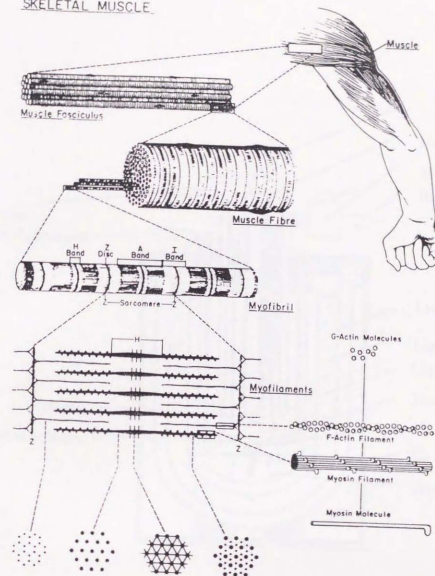
Figure 1: **Schematic Diagram of Micro-Anatomy of Skeletal Muscle**
This figure shows the schematic diagram of skeletal muscle and its consisting components (From Bagshaw,C.R., 1982).

plug

sample introducing tube

three–sided valve
Helium collection tube

Helium transfer tube

Liquid N$_2$ entrance

Liquid N$_2$ dewar vessel

Liquid N$_2$

Liquid Helium dewar vessel

Thermocouple

Cu block(exchangable)

shutter

thermal reflector

Cu block(fixed)

Liquid Helium
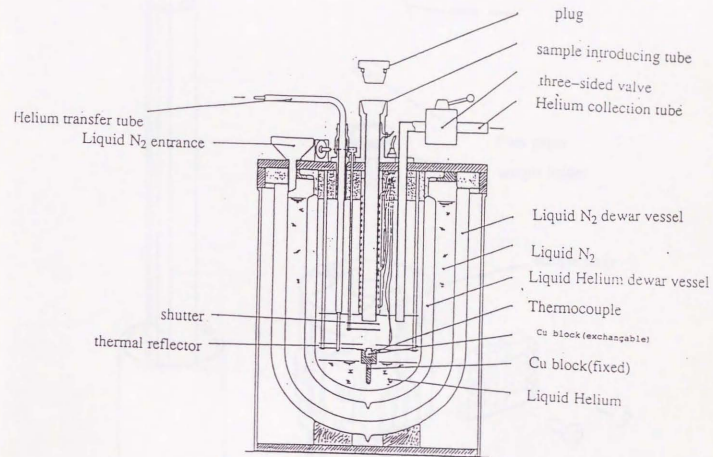
Figure 2: **The apparatus for rapid-freezing**
The cross-sectional view of the apparatus for rapid-freezing(RF-10A, Eiko engineering) was shown. From the sample introducing tube, the plunger (Figure 3) was introduced to press a specimen against copper block. The copper block is exchangeable, so that the surface of the block can be kept clean.

36

plunger

sample(muscle fibre)

T-clip

cotton thread

filter paper

sample holder

sample stage
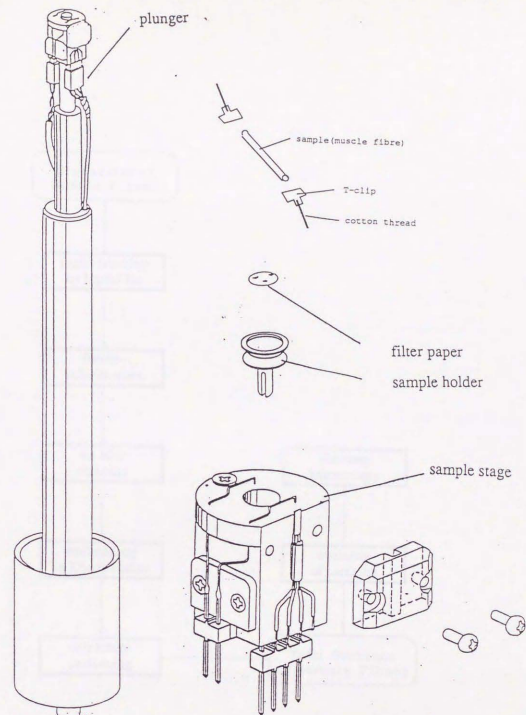
Figure 3: **Schematic Diagrams of Plunger for Rapid-Freezing**
This is the schematic drawing of plunger which is originally made by Eiko engineering and modified by T. Akiba(T. Akiba, 1985). By this plunger, the specimen was pressed on the exchangeable copper block which is in the apparatus for rapid-freezing.

37
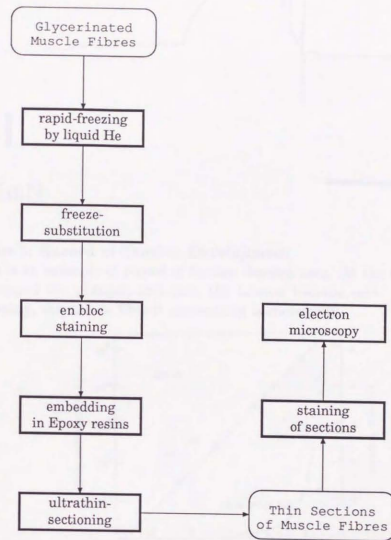
Figure 4: **Schematic Diagrams of Specimen Preparation**
This is the schematic drawing of process of preparation of specimen done in this experiment. By this process, thin sections of muscle fibres could be obtained and then they were observed by electron microscopy.

1mN

1min
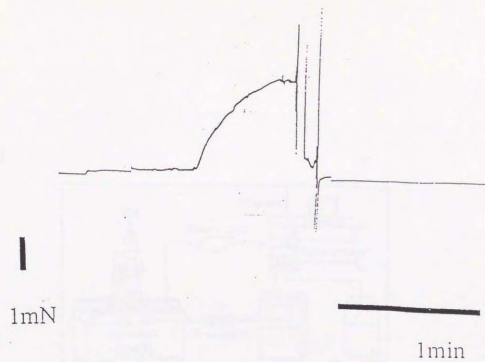
Figure 5: **Record of Tension Development**
This is an example of record of tension development. At the maximum force,
I dropped the plunger, and then the tension became zero. At the time of
dropping, the muscle fibre is contracting isometrically.
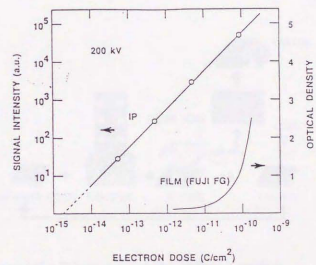
Figure 6: **Characteristics of Imaging Plates Used by Electron Microscopy**
This graph shows intensity of the IP vs. electron dose responses. From this
graph, high sensitivity and wide dynamic range with exact linearity are clearly
seen. (From Mori,N., *et al.*, 1990)

39

(a)
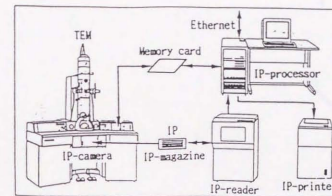
(b)
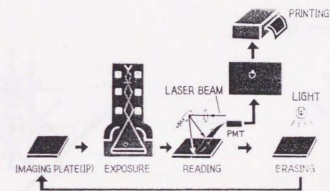
Figure 7: **Schematic Diagram of the PIXsysTEM**
(a) This is the schematic diagram of the PIXsysTEM(JEOL), which I used for
measurement of electron micrographs with Imaging Plate(IP). (b) Schematic
diagram of processes of recording, reading, and erasing an image on the IP.
(From Oikawa,T., *et al.*, 1990)
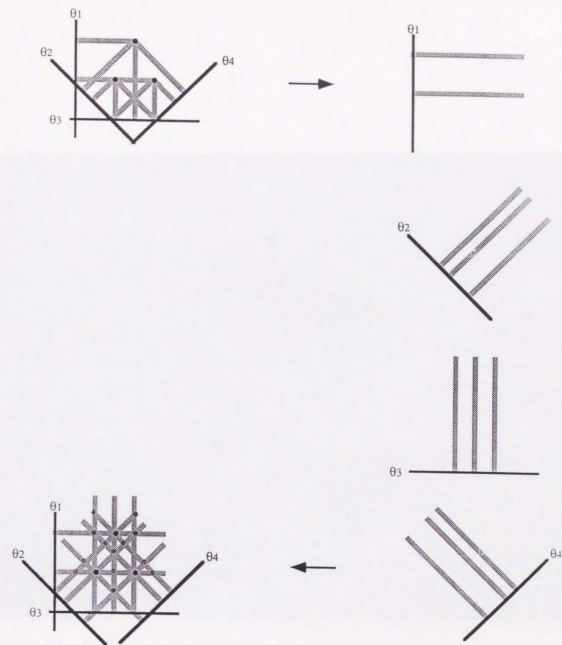
Figure 8: **Principle of a Simple Back-Projection**
A binary object consisting of three points (a) is projected onto five projections
P at an angles θ_1, θ_2, θ_3, and θ_4. (b) From these projections, back-projection
bodies B are created and the object is reconstructed by addition of these back-
projection bodies (c). (From Radamacher,M.., 1992)

41

_____ 1 μm

Figure 9: **Low Magnification Image of a Contracting Muscle Fibre**
To examine the extent of the preservation of muscle fibres in freezing, the image of the direct magnification of 10,000× was recorded. The region which is under 2 μm from the region is well preserved, but in the lower region, one can see the damage by freezing. The contact surface to copper block was specified by arrows.

42
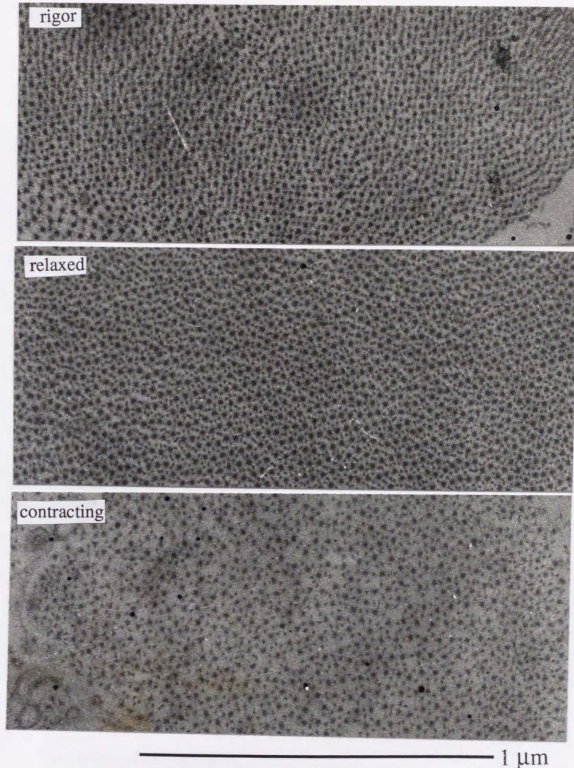
Figure 10: **Images of Muscle Fibres in Various States**
This figure shows muscle fibres in various states. These photographs are taken using films with electron dose of about $10 \ e/\text{Å}^2$. Thus these figures have high signal-to-noise ratio compared to other figures shown below. In this figure, darker areas represent filaments, or proteins. Photographs in rigor and contracting state are somewhat resemble, while in relaxed state the thick filaments are thicker than they in rigor and contracting state. Furthermore, background region between thick filaments and thin filaments are clear with little cross-bridges.

43
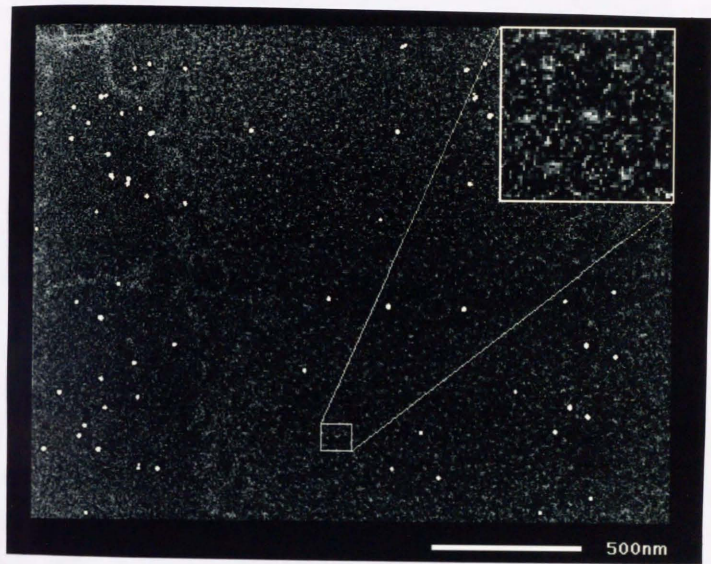
Figure 11: **Image of a Contracting Muscle Fibre Used for Reconstruction**
This is the region used for three-dimensional reconstruction. The direct magnification was 50,000×. The inset is the magnified image of the rectangular region of lower centre. One can see the hexagonal lattice of thick filaments (marked). Thin filaments are also positioned on a hexagonal lattice but it is difficult to be distinguished from noise. In these views, the proteins are represented brighter than the background.

44
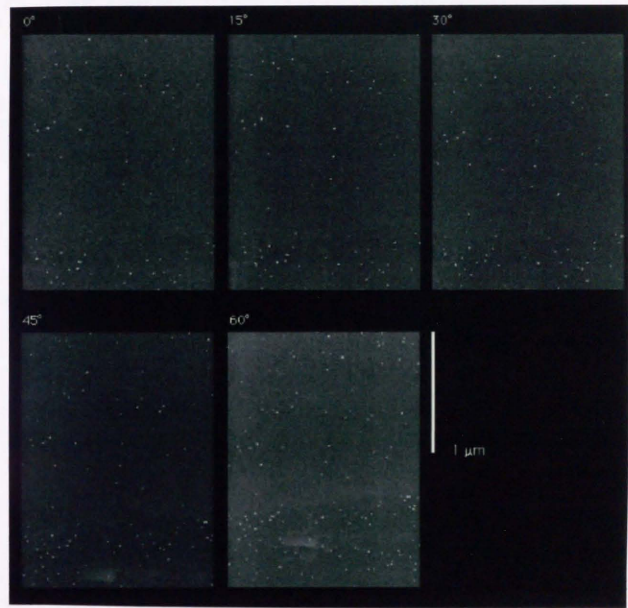
Figure 12: **Various Tilted Images of Sections with Fiducial Markers**
I show tilt series of sections. One can estimate the tilting angles by the position of colloidal gold markers which can be seen as dark spots in this figure. The tilting axis is from right to left approximately. The typical three spots are connected by lines to show the tilting angles of the planes by deformation of the triangle.

45
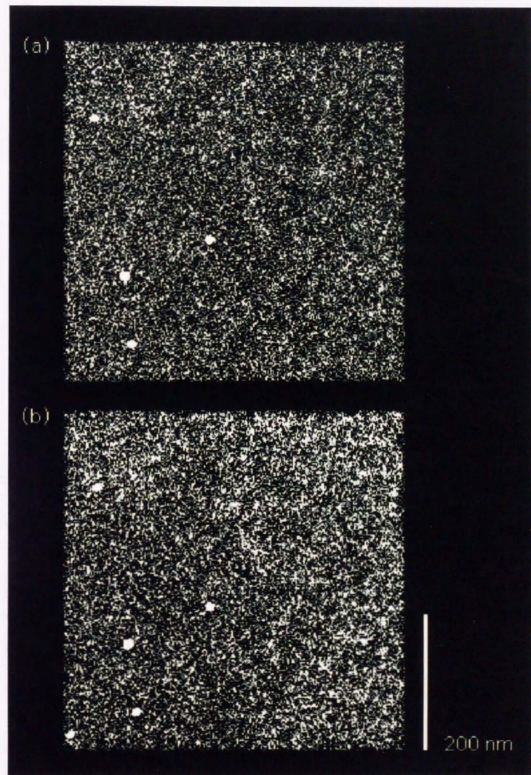
Figure 13: **Comparison of Non-Tilt Images in the First Photographs and the Last Photographs**
These two images were non-tilt views in the first photographs and the last photographs in a tilt-series. There is difference of the values in background. One can see the "clearing" effect of background by electron radiation, although it can be seen that there is no significant difference in proteins. (a) The first image. (b) The last image.
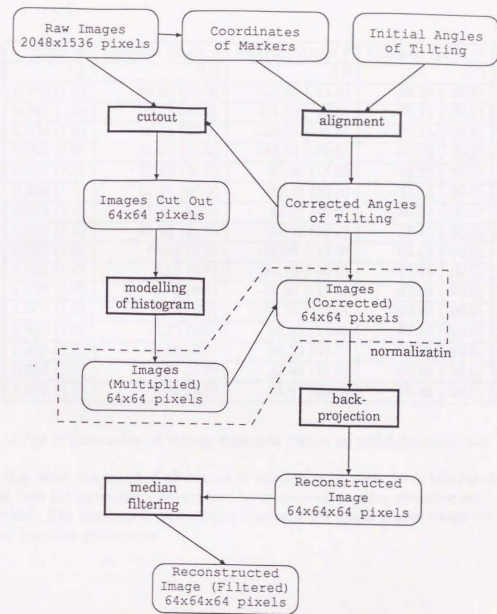
Figure 14: **Schematic Diagram of Image Processing**
This is the schematic diagram of image processing used in this experiment.
By this image processing, the three-dimensional reconstruction of contracting
muscle fibres can be obtained.
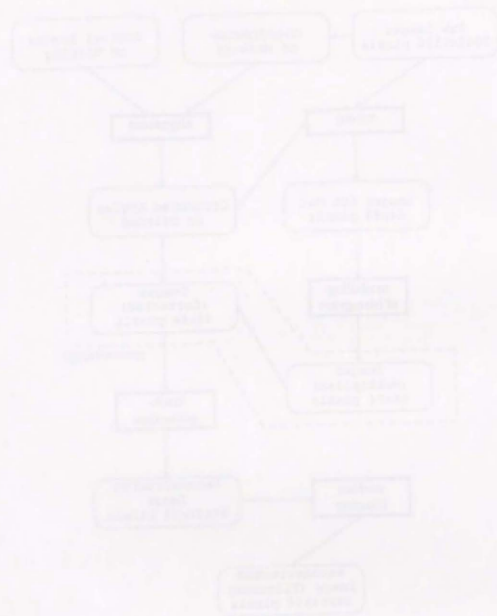
Scale m	Eulerian Angle ϕ	Eulerian Angle θ	Eulerian Angle ψ
1.0	0.0	0.0	0.0
0.996 (1.0)	88.03 (90.0)	-14.40 (-15.0)	-87.29 (-90.0)
0.997 (1.0)	79.08 (90.0)	-31.75 (-30.0)	-78.41 (-90.0)
0.994 (1.0)	80.14 (90.0)	-46.67 (-45.0)	-79.74 (-90.0)
1.003 (1.0)	81.03 (90.0)	-63.88 (-60.0)	-80.30 (-90.0)
0.997 (1.0)	75.22 (90.0)	12.55 (15.0)	-74.56 (-90.0)
0.998 (1.0)	81.51 (90.0)	25.82 (30.0)	-81.43 (-90.0)
0.999 (1.0)	81.29 (90.0)	40.68 (45.0)	-80.84 (-90.0)
1.004 (1.0)	81.90 (90.0)	55.29 (60.0)	-81.41 (-90.0)
0.997 (1.0)	18.08 (0.0)	-16.88 (-15.0)	-93.05 (-90.0)
1.001 (1.0)	7.19 (0.0)	-31.73 (-30.0)	-82.79 (-90.0)
1.006 (1.0)	6.73 (0.0)	-46.90 (-45.0)	-82.58 (-90.0)
1.007 (1.0)	6.73 (0.0)	-62.15 (-60.0)	-82.82 (-90.0)
0.999 (1.0)	-7.33 (0.0)	12.50 (15.0)	-67.16 (-90.0)
0.999 (1.0)	3.46 (0.0)	28.55 (30.0)	-78.00 (-90.0)
0.992 (1.0)	5.31 (0.0)	42.99 (45.0)	-80.45 (-90.0)
1.003 (1.0)	5.45 (0.0)	58.37 (60.0)	-80.30 (-90.0)

Table 1: Correction of Tilting Angles of Planes on which Sections Are

In this table, the result of alignment of colloidal gold particles is tabulated. The final tilt parameters determined by minimization using direction set method. The numbers in parenthesis represent the initial angles which are read from the goniometer.

48

(a)

	calculated x-position (observed)	calculated y-position (observed)
mark0	327.33 (325.09)	156.76 (157.99)
mark1	444.29 (444.16)	407.00 (406.67)
mark2	407.31 (408.92)	514.12 (514.60)
mark3	209.77 (207.91)	478.86 (478.95)
mark4	225.61 (226.89)	267.22 (267.08)
mark5	168.45 (169.71)	257.95 (257.06)
mark6	175.08 (175.14)	162.44 (162.00)

(b)

	calculated z-coordinate	z-coordinate on the plane
mark0	4.38	5.30
mark1	4.88	3.00
mark2	1.45	-0.16
mark3	-4.14	-4.42
mark4	-1.47	0.42
mark5	-3.37	-0.83
mark6	-1.68	1.34

Table 2: Example of Calculated Coordinates of Fiducial Markers

The calculated coordinates of markers from the 60° tilted image were
compared with the observed coordinates on non-tilted image. The deviation
from z-direction of markers was included in the processing of alignment,
therefore, it can be also estimated whether the markers are on a plane or not.
(a) An Example of Coordinates of markers measured and projected from the
calculated three-dimensional position. (b) Errors in z-direction assuming that
fiducial markers are in the same plane. The numbers are representing pixel
values.

49

Figure 15: **Fitting of Gaussian Curves to Histogram of Densities**
This figure shows the result of modelling of the histogram by addition of two
Gaussian curves. (a) The image is not tilted. (b) The image is tilted by 60°.

50
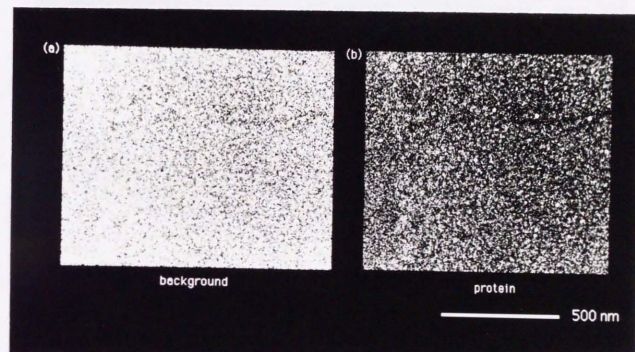
Figure 16: **Images with Cutoff Determined by Fitting to Gaussian Curves**

Images with cutoff levels determined by average and standard deviation of the fitted Gaussian curves were shown. In these views, proteins are brighter than background. (a) This figure shows the image with cutoff levels corresponding to background. (b) This figure shows the image with cutoff levels corresponding to proteins.

51
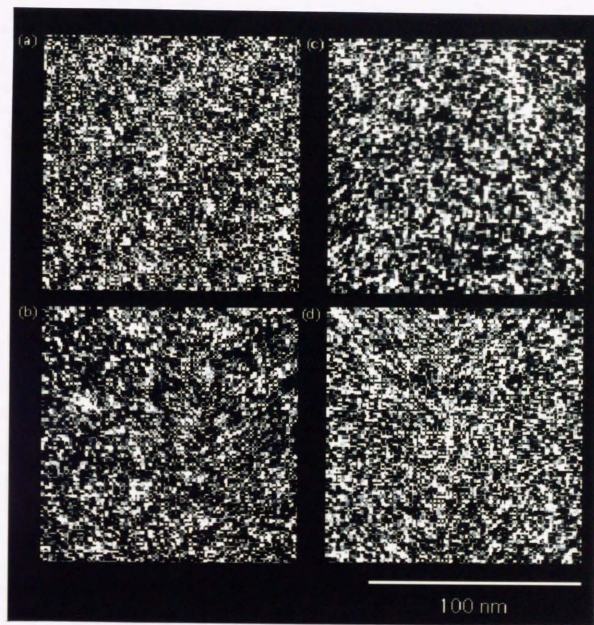
Figure 17: **Original Images I used for Three-Dimensional Reconstruction**

This figure shows examples of images cut out from the observed image by bicubic spline interpolation and normalized using fitting parameter of modelling of the histogram by addition of two Gaussian curves. Because very low electron dose causes the low signal-to-noise ratio of observed images, images cut out are also noisy. Thus it is difficult to distinguish thick filaments and thin filaments in this enlarged images. Proteins are brighter than background in these views.
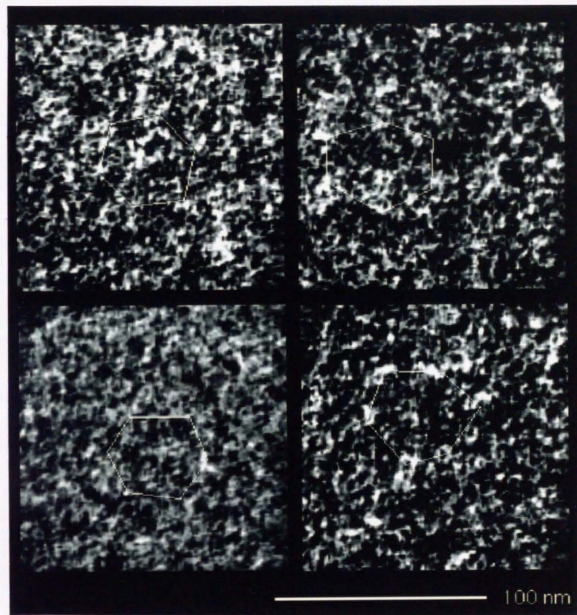
Figure 18: **Three-Dimensional Image Reconstructed by Simple Back-Projection**
This figure shows a slice of the three-dimensional images reconstructed by simple back-projection method. The size of slices are 74 nm × 74 nm. Each slice has little noise compared with the original images in tilt series, because noises are cancelled out in back-projection process. Thus signal-to-noise ratio was improved.

53
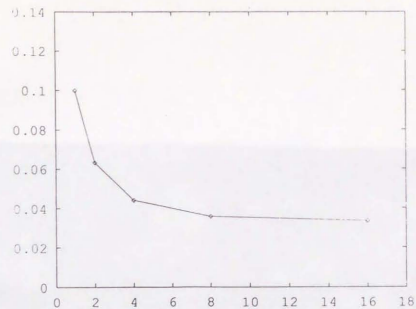
Figure 19: **Values of r between Projections of the Reconstructed Image and the Observed Images in Tilt Series**
This graph show the r values calculated from projections of the reconstructed Image and the photographed images in tilt series taken in this order. There is no tendency to increase the r values. This means that damage by electron radiation can be neglected in this resolution (1 nm pixel).

[cumulative electron dose]
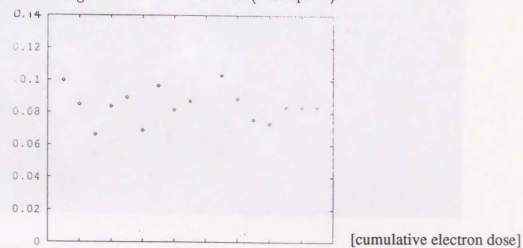
Figure 20: **Values of r in the Reconstructed Image at Various Resolution**
This graph lists the r value between projections of the reconstructed image and the observed images that are averaged to the listed size with each pixel. Thus, I can estimate the resolution of the reconstructed image as about 8 nm, because the r value increases steeply with better resolution.

54
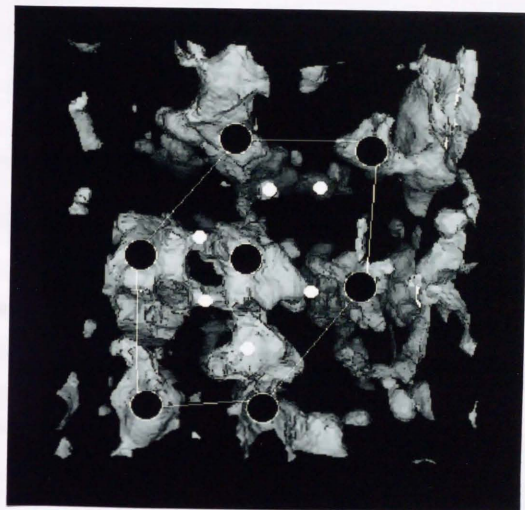
Figure 21: **Three-Dimensional Median-Filtered Reconstructed Image**
A shaded view of the three-dimensionally reconstructed images after median-filtering are shown. In this view, thick filaments and cross-bridges protruding from the thick filaments can be seen. The entire thin filaments, on the other hand, cannot be observed, although those near cross-bridges can be identified. Thus the estimated position of thick and thin filaments are schematically over this shaded view. Large black circles correspond to thick filaments and small white circles correspond to thin filaments.
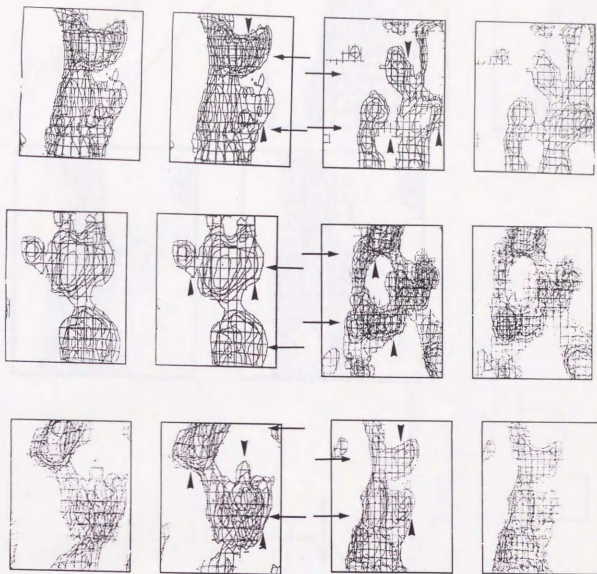
Figure 22: **Gallery of Thick Filaments of the Reconstructed Images**
This figure shows stereo views of the reconstructed thick filaments in various
region. In these images, the 14.3 nm pitch of myosin heads are clearly seen
and this pitch is represented by arrows. Arrow heads are corresponding to the
densities of myosin heads protruding to the direction of a thin filament. The
direction of M-line is upward.

56
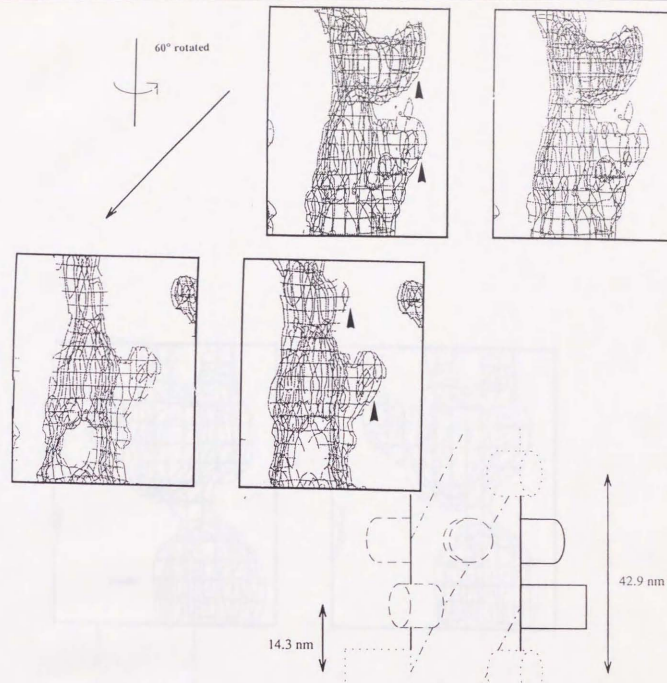
Figure 23: **Stereo Views of a "Tapole-like" Cross-bridge in Contracting Muscle Fibres**

This figure shows stereo views of an example of "tadpole-like" cross-bridges in the reconstructed images. The shape of these cross-bridges, which are represented by arrow-head, closely resemble the shape of cross-bridges of muscle fibres in rigor state (Taylor,K., 1989). In these cross-bridges, there will be two myosin heads. The schematic drawing of this thick filament and cross-bridges are shown under the stereo view. The broken lines represent that the cross-bridges of those region are near thick filaments and they could not be seen. This schematic drawing shows that the cross-bridges are protruding to thin filaments according to the helical symmetry of the thick filament.
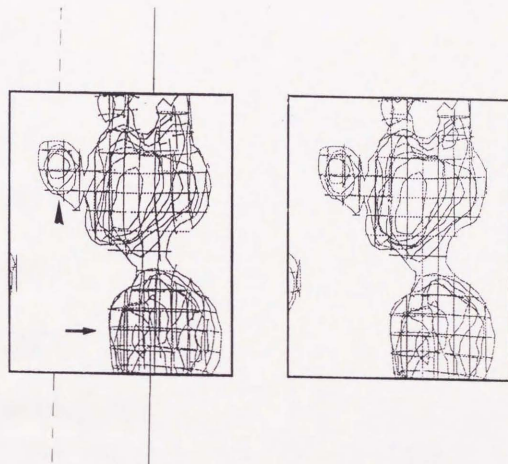
Figure 24: **Stereo View of Other Types of Myosin Heads**
This figure shows stereo views of other types of myosin heads which differ to the myosin heads in "tadpole-like" cross-bridges. In this stereo view, the myosin heads, which are very close to a thick filament and cannot be distinguished to the thick filament, are indicated by an arrow. On the other hand, the cross-bridge containing one myosin head is pointed out by an arrowhead. The thick filament was represented by continuous lines and the thin filament, which could not be reconstructed, was represented by broken lines.

58